Adiabatic RF Pulses

Robin A. de Graaf

Yale University, New Haven, CT, USA

Adiabatic radio frequency pulses are amplitude- and frequency (or phase)-modulated RF pulses with a high immunity to RF inhomogeneity and frequency offsets. The adiabatic condition, which governs the rotation of the magnetization during an adiabatic RF pulse, is explained graphically. Thereafter, the effects of different amplitude- and frequency modulation functions are demonstrated. The inversion and refocusing properties of adiabatic full-passage pulses are discussed in detail. This article concludes by showing the utility of adiabatic RF pulses in a number of in vivo magnetic resonance spectroscopy applications related to spatial localization, outer volume suppression, and broadband decoupling.

Keywords: adiabatic RF pulse, adiabatic full passage, RF inhomogeneity, off-resonance performance, spatial localization, broadband decoupling

How to cite this article:
eMagRes, 2016, Vol 5: 1003–1014. DOI 10.1002/9780470034590.emrstm1443

Introduction

Radio frequency pulses are at the heart of every magnetic resonance (MR) experiment. They are the principle tools to achieve spin manipulations like excitation, inversion, and refocusing. The range of RF pulse types is enormous and can include RF amplitude, frequency, and gradient modulations. The majority of MR experiments are performed with conventional, amplitude-modulated RF pulses, which include hard (i.e., square or unmodulated), Gaussian, sinc, and optimized Shinnar-Le Roux (SLR)[1] pulses. When used in combination with volume resonators that are characterized by a relatively homogeneous RF transmit field, amplitude-modulated RF pulses provide excellent results. However, the nutation angle of amplitude-modulated RF pulses is linearly dependent on the RF transmit field strength, B_1. As such, their performance strongly degrades when used in combination with surface coils that allow more sensitive signal detection, and are also characterized by an inhomogeneous RF transmit field. The spatially varying nutation angle can lead to signal loss, undesired image contrast and artifacts.

This short overview is focused on adiabatic RF pulses that have simultaneous amplitude and frequency modulation. This seemingly minor modification has major consequences on pulse performance. Adiabatic RF pulses have an extreme tolerance to variations in RF amplitude. In addition, adiabatic RF pulses have been shown to provide superior off-resonance performance. Taken together, adiabatic RF pulses can provide a convenient, user-friendly option to ensure maximum performance in a wide range of experiments. While there is still continuing development of adiabatic RF pulses, it should be realized that their concept has been utilized since the very first NMR experiments by Bloch[2] and Purcell *et al.*[3] who used adiabatic full (or fast) passage (AFP) for magnetization inversion.

The theoretical principles of adiabatic RF pulses have been reviewed in detail.[4–6] Here, we focus on their practical implementation, calibration, and applications. Following a brief section on the theoretical foundations of adiabatic RF pulses, emphasis is given to the choice of modulation functions and their effect on off-resonance performance. The utility of adiabatic RF pulses is demonstrated by three in vivo MR spectroscopy (MRS) applications.

Theory

Modulation Functions

The amplitude $B_1(t)$ and frequency $\Delta\nu(t)$ modulations of adiabatic RF pulses can be described in a constant phase, frequency-modulated (FM) reference frame as

$$B_1(t) = B_{1,\max} f_B(t) \tag{1}$$

$$\nu(t) - \nu_c = \Delta\nu(t) = \nu_{\max} f_\nu(t) \tag{2}$$

where $B_{1,\max}$ and $\nu_{\max}$ are the maximum RF amplitude and maximum frequency offset (in Hz), respectively, and ν_c the RF carrier frequency (in Hz). Note that some previous publications use angular frequency $\Delta\omega(t) = 2\pi\Delta\nu(t)$, instead. For convenience, both $B_1(t)$ and $\Delta\nu(t)$ are expressed in units of Hz. The Larmor equation can be used to convert units from Tesla and Hertz, for example, B_1 (in T) $= (2\pi/\gamma)B_1$ (in Hz), where γ is the gyromagnetic ratio (in rad T^{-1} s^{-1}). One of the most common adiabatic RF pulses is the hyperbolic secant (HS1) pulse[7,8] for which the modulations are given by

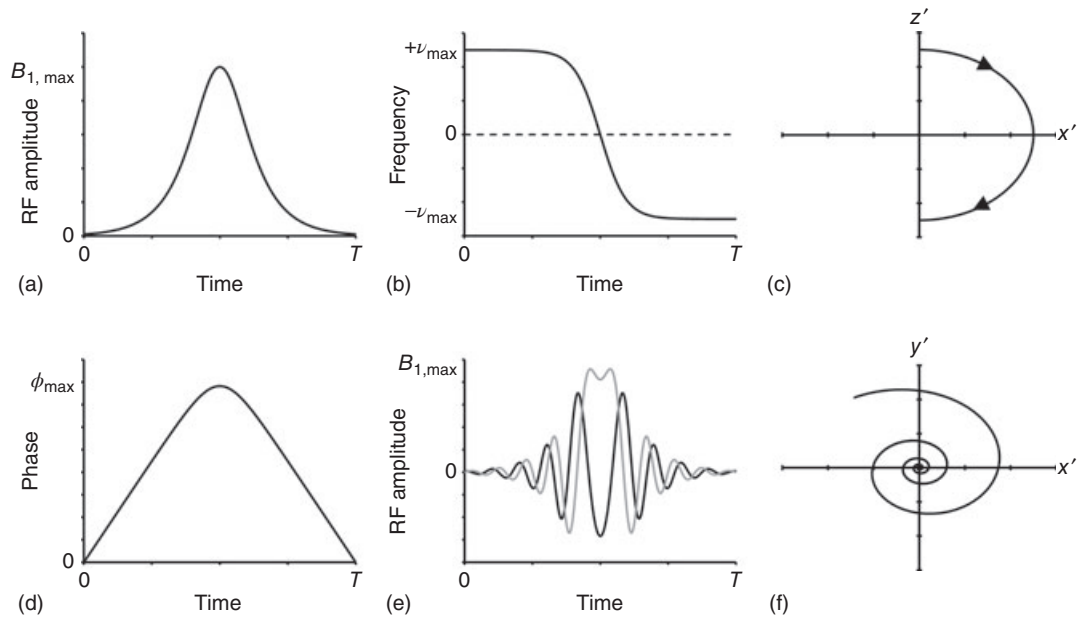

Figure 1. (a) Amplitude and (b) frequency modulation functions for a hyperbolic secant (HS1) adiabatic RF pulse. (c) Rotation of the effective field in a frequency-modulated (FM) frame in which the orientation of $B_1(t)$ is constant along x'. (d) Phase modulation function as calculated from (b) using equation (5). (e) Real (black, B_{1x}) and imaginary (gray, B_{1y}) components of $B_1(t)$. (f) Rotation of the B_1 field in a constant-frequency, phase-modulated (PM) frame

$$B_1(t) = B_{1,\max}\text{sech}\,(\beta\,(1 - 2t/T)) \qquad (3)$$

$$\Delta\nu(t) = \nu_{\max}\tanh(\beta(1 - 2t/T)) \qquad (4)$$

where T is the pulse length and $0 \le t \le T$. β is a dimensionless truncation factor that is typically defined as $\text{sech}(\beta) = 0.01$. Figure 1(a) and (b) shows the RF modulations as defined by equations (3) and (4). Figure 1(c) shows the trajectory of the effective field $B_e(t)$, which represents the vector sum of $B_1(t)$ and $\Delta\nu(t)$. It follows that in the FM frame, the orientation of the $B_1(t)$ field remains stationary along the x'-axis, whereas the $B_e(t)$ field rotates from the $+z'$-axis through the $+x'$-axis onto the $-z'$-axis.

On most modern spectrometers, adiabatic RF pulses are implemented as amplitude and *phase*-modulated (PM) RF pulses. The frequency and phase modulations are closely related as phase is the time integral of frequency according to

$$\phi(t) = 2\pi \int_0^t \Delta\nu(t)\mathrm{d}t \qquad (5)$$

which, for an HS1 pulse evaluates to

$$\phi(t) = \frac{\pi\nu_{\max}T}{\beta}\ln\left[\frac{\text{sech}\,(\beta\,(1 - 2t/T))}{\text{sech}(\beta)}\right] \qquad (6)$$

Figure 1(d) shows the HS1 phase modulation given by equation (6). The derivation of a closed-form expression for the phase modulation based on other frequency modulation functions $f_\nu(t)$ may not always be possible. In general, a closed-form expression is not required as the phase modulation can be obtained through numerical integration according to equation (5). In a constant-frequency PM reference frame, the trajectory of the RF field can be described by two magnetic fields $B_{1x}(t)$ and $B_{1y}(t)$, along the x and y axes, respectively, given by $B_{1x}(t) = B_1(t)\cos\phi(t)$ and $B_{1y}(t) = B_1(t)\sin\phi(t)$ and are shown in Figure 1(e). Figure 1(f) shows the trajectory of the $B_1(t)$ field in the PM frame. Whereas adiabatic RF pulses are experimentally executed with amplitude and phase modulation, the principles of adiabatic RF pulses and their effect on the magnetization are best understood in the FM frame with amplitude and frequency modulation.

Adiabatic Condition

So far, only the magnetic fields associated with the adiabatic RF pulses have been considered. However, the ultimate purpose of AFP pulses is to invert the longitudinal magnetization. Figure 2 shows the modulation of the magnetization during an HS1 AFP pulse in the FM frame $x'y'z'$. At the onset of the pulse, the effective field $B_e(0)$ is equal to the frequency offset $\nu_{\max}$ along the $+z'$-axis. The longitudinal magnetization is parallel to $B_e(0)$. As the pulse is executed according to the modulations shown in Figure 1(a) and (b), the frequency offset decreases and the RF field along the x'-axis increases, rotating the effective field $B_e(t)$ away from the $+z'$-axis. As long as the effective field is rotating slowly compared to its amplitude, the longitudinal magnetization will remain parallel to $B_e(t)$ and therefore follows $B_e(t)$. Halfway through the pulse, both $B_e(T/2)$ and the magnetization have been rotated to the x'-axis. If the pulse is terminated at this point in time, it is referred to as an adiabatic half-passage (AHP) pulse and it has achieved excitation. When the AFP pulse is continued, the effective field is rotated toward the $-z'$-axis, ultimately resulting in an inversion of the magnetization.

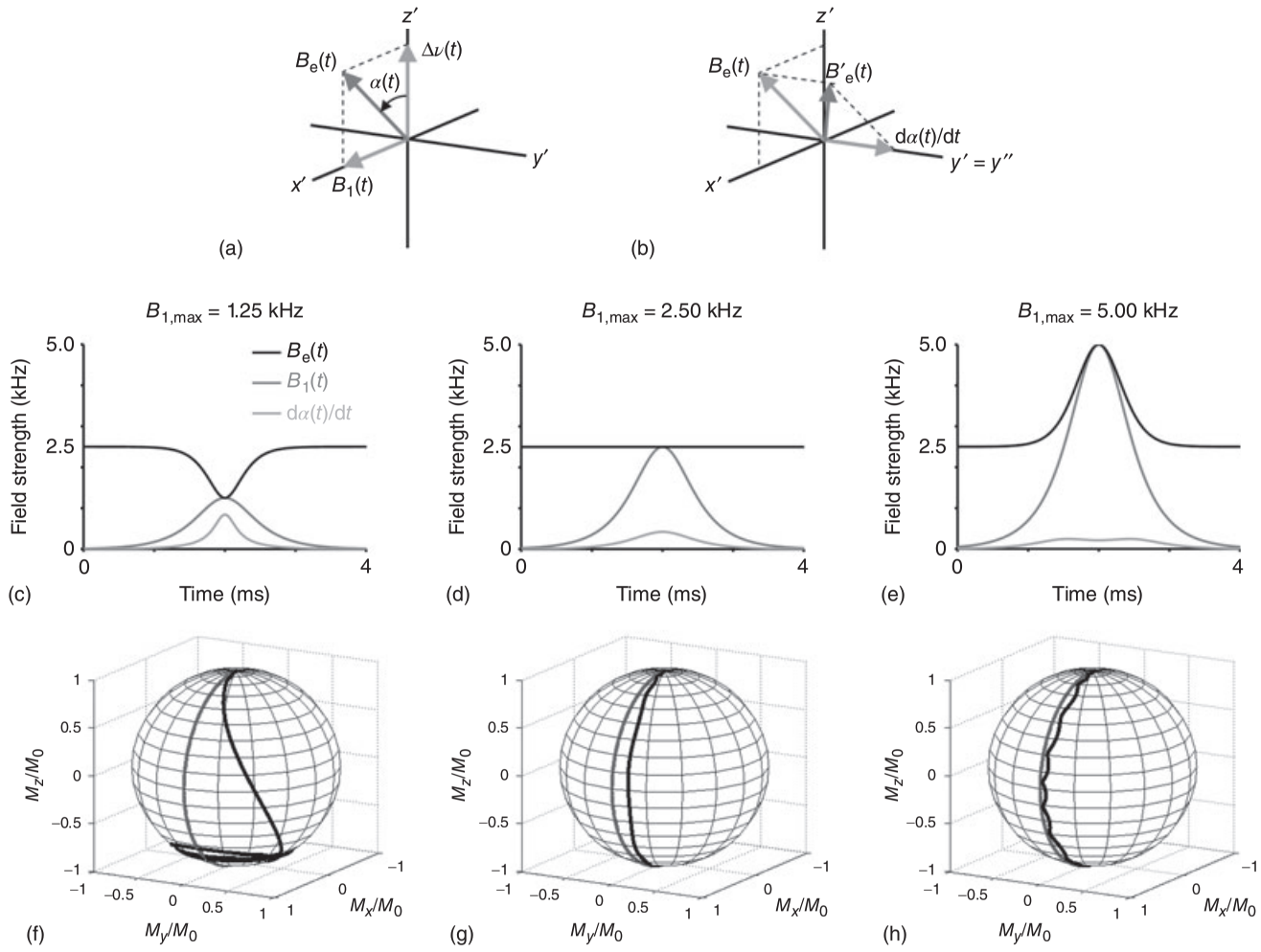

Figure 2. (a) Magnetic field components in a FM frame-of-reference $x'y'z'$. (b) Magnetic field components in a secondary frame-of-reference $x''y''z''$, which rotates around the $y' = y''$-axis with frequency $[d\alpha(t)/dt]$. $B_e(t)$ starts and remains along the z''-axis (not shown). (c–e) Temporal evolution of $B_e(t)$, $B_1(t)$, and $[d\alpha(t)/dt]$ during a 4-ms HS1 pulse ($R = 20$) at maximum RF amplitudes $B_{1,max}$ of (c) 1.25 kHz, (d) 2.50 kHz, and (e) 5.00 kHz. (f–h) Temporal evolution of the longitudinal magnetization during the same 4.0 ms HS1 ($R = 20$) pulse. At a $B_{1,max}$ of (f) 1.25 kHz, the adiabatic condition of equation (7) is not sufficiently satisfied leading to incomplete inversion. At $B_{1,max}$ of (g) 2.50 kHz and (h) 5.00 kHz, the adiabatic condition is satisfied throughout the pulse leading to a near-complete inversion

The primary requirement for the magnetization to remain parallel with $B_e(t)$ is that the effective field rotates slowly. The rate of change of $B_e(t)$ is equal to $d\alpha(t)/dt$, where $\alpha(t)$ is the angle between $B_e(t)$ and the z'-axis (Figure 2a). In a rotating frame of reference in which the orientation of $B_e(t)$ is always along z'', the rate of change in $B_e(t)$ can be represented as a vector along the y''-axis (Figure 2b). The $B_e(t)$ and $d\alpha(t)/dt$ vectors together make up a total effective field $B_e'(t)$ around which the magnetization is precessing. When the rate of change $d\alpha(t)/dt$ is small compared to $B_e(t)$, the $B_e(t) \sim B_e'(t)$ and the magnetization follows the effective field as described earlier. When $d\alpha(t)/dt$ is relatively large compared to $B_e(t)$, $B_e'(t)$ significantly deviates from $B_e(t)$ leading to erratic rotations of the magnetization around $B_e'(t)$.

A rotation is said to be adiabatic when $B_e(t) \sim B_e'(t)$ throughout the pulse, which can be represented by the inequality:

$$\left|B_e(t)\right| = \sqrt{B_1^2(t) + \Delta\nu^2(t)} \gg \left|\frac{d\alpha(t)}{dt}\right| \tag{7}$$

with

$$\alpha(t) = \text{atan}\left(\frac{\Delta\nu(t)}{B_1(t)}\right) \tag{8}$$

Equation (7) is commonly referred to as the 'adiabatic condition' and has been extensively used in the design and optimization of modulation functions for AFP pulses.[9,10] Using the vector diagrams and equation (7), it is now straightforward to understand the high immunity of adiabatic RF pulses to RF inhomogeneity. Figure 2(c–e) shows the RF modulation $B_1(t)$, effective field $B_e(t)$, and rate of change $d\alpha(t)/dt$ during an HS1 pulse for various RF amplitudes. For a maximum RF amplitude $B_{1,max}$ of 1.25 kHz, it is clear from Figure 2(c) that $|B_e(t)| \sim |d\alpha(t)/dt|$ for a significant part of the pulse when $t \sim T/2$. As a result, the magnetization rotates around $B_e'(t)$, which significantly deviates from $B_e(t)$, leading to erratic modulations of the magnetization as shown in Figure 2(f). In other words, a 4 ms HS1 pulse with a 2.5 kHz maximum frequency modulation does not adequately satisfy the adiabatic condition of equation (7) at $B_{1,max} = 1.25$ kHz thereby leading to an incomplete inversion. The situation for $B_{1,max} = 2.5$ kHz (Figure 2d and g) and 5.0 kHz (Figure 2e and h) is significantly different in that the magnetization largely follows the effective field from the $+z$ to the $-z$-axis. Figure 2(d) and (e) reveals that $|B_e(t)| \gg |d\alpha(t)/dt|$ throughout the pulse, ensuring complete inversion. From Figure 2, it should be clear that an increase in $B_{1,max}$ leads to different $B_e(t)$ and $d\alpha(t)/dt$ modulation curves, but as long as $|d\alpha(t)/dt| \ll |B_e(t)|$ throughout the RF pulse, the magnetization follows the effective field, thereby resulting in inversion.

Using tools identical to those shown in Figure 2, that is, vector diagrams and equation (7), it is straightforward to show that HS1 AFP pulses only achieve inversion for frequency offsets ν that satisfy $-\nu_{max} \le \nu \le \nu_{max}$, that is, the inversion profile is frequency selective. For frequency offsets $\nu > \nu_{max}$, the effective field $B_e(t)$ rotates away from the $+z'$-axis as $\Delta\nu(t)$ decreases and $B_1(t)$ increases. However, as $\nu(t) - \nu > 0$ throughout the pulse, the effective field never crosses the transverse plane. Instead, $B_e(t)$ rotates back toward the $+z'$-axis. When the adiabatic condition is adequately satisfied, the magnetization follows $B_e(t)$ as it rotates away from and then back to the $+z'$-axis, leading to an effective rotation of 0° at the end of the pulse.

Tannus and Garwood used the adiabatic condition of equation (7) to derive a general class of adiabatic modulation functions that satisfy the adiabatic condition equally for all frequencies $|\nu| \le |\nu_{max}|$. The details of these so-called offset-independent adiabaticity (OIA) modulation functions can be found in Refs 10, 11. One of the most useful groups of OIA pulses is the HSn family, which can be described by:

$$B_1(t) = B_{1,max}\,\text{sech}\left(\beta(1 - 2t/T)^n\right) \tag{9}$$

$$\Delta\nu(t) = \Delta\nu_{max}\left[1 - 2\left(\int_0^t f_b^2(t)\,dt \Big/ \int_0^T f_b^2(t)dt\right)\right] \tag{10}$$

where n is an integer. Note that for $n = 1$, the pulse reduces to the HS1 pulse described earlier. Once the adiabatic condition is satisfied, OIA pulses have some common features that include a constant inversion profile for $|\nu| \le |\nu_{max}|$ and an identical average B_1 field, $B_{1,rms}$ for the minimum $B_{1,max}$, necessary to achieve inversion. The point at which the adiabatic condition is satisfied varies widely among OIA and other AFP pulses.

Figure 3 shows the performance of three AFP pulses over a range of B_1 amplitudes and frequency offsets. Figure 3(c–e) and (h–j) shows the performance of the OIA pulses HS1 (Figure 3a and b) and HS8 (Figure 3f and g) with different R values, where $R \equiv 2\Delta\nu_{max}T$. Figure 3(m–o) shows the performance of an optimized AFP pulse (Figure 3k and l) that can be described by:

$$B_1(t) = B_{1,max}\tanh\left(\xi\left(1 - |1 - 2t/T|\right)\right) \tag{11}$$

and

$$\Delta\nu(t) = \nu_{max}\tan\left(\kappa\left(1 - 2t/T\right)\right) / \tan\left(\kappa\right) \tag{12}$$

which for $\xi = 10$ and $\kappa = \text{atan}(20)$ closely resembles an AFP pulse with numerically optimized modulation (NOM) functions optimized to give the largest bandwidth at the lowest RF amplitude.[9,12]

From Figure 3, it follows that HS1 and HS8 pulses both achieve OIA at $R \ge 40$. The HS8 pulse achieves good performance at $B_{1,max} \sim 1.3$ kHz, whereas the HS1 pulse requires $B_{1,max} \sim 2.5$ kHz to achieve the same inversion. When the different amplitude modulation functions are taken into account, the average RF amplitude $B_{1,rms}$ is roughly similar for both pulses. The HS8 pulse is therefore a good choice when the maximum RF amplitude is limited, whereas the HS1 provides a sharper inversion profile with narrower transition bands. At low R values, the HS8 pulse does not adequately satisfy the adiabatic condition, making the HS1 pulse the only valid choice. The AFP pulse described by equations (11) and (12) behaves very differently from the HS1 and HS8 pulses. Even though the minimum R value to achieve adequate performance is much higher, the pulse performs well at relatively low $B_{1,max}$. In addition, while HS1 and HS8 achieve frequency-selective inversion independent of the applied RF amplitude, the inversion bandwidth of the NOM AFP pulse increases with increasing $B_{1,max}$. This is because the NOM AFP pulse does not exhibit OIA. As a result, the NOM AFP pulse is an excellent choice for inversion

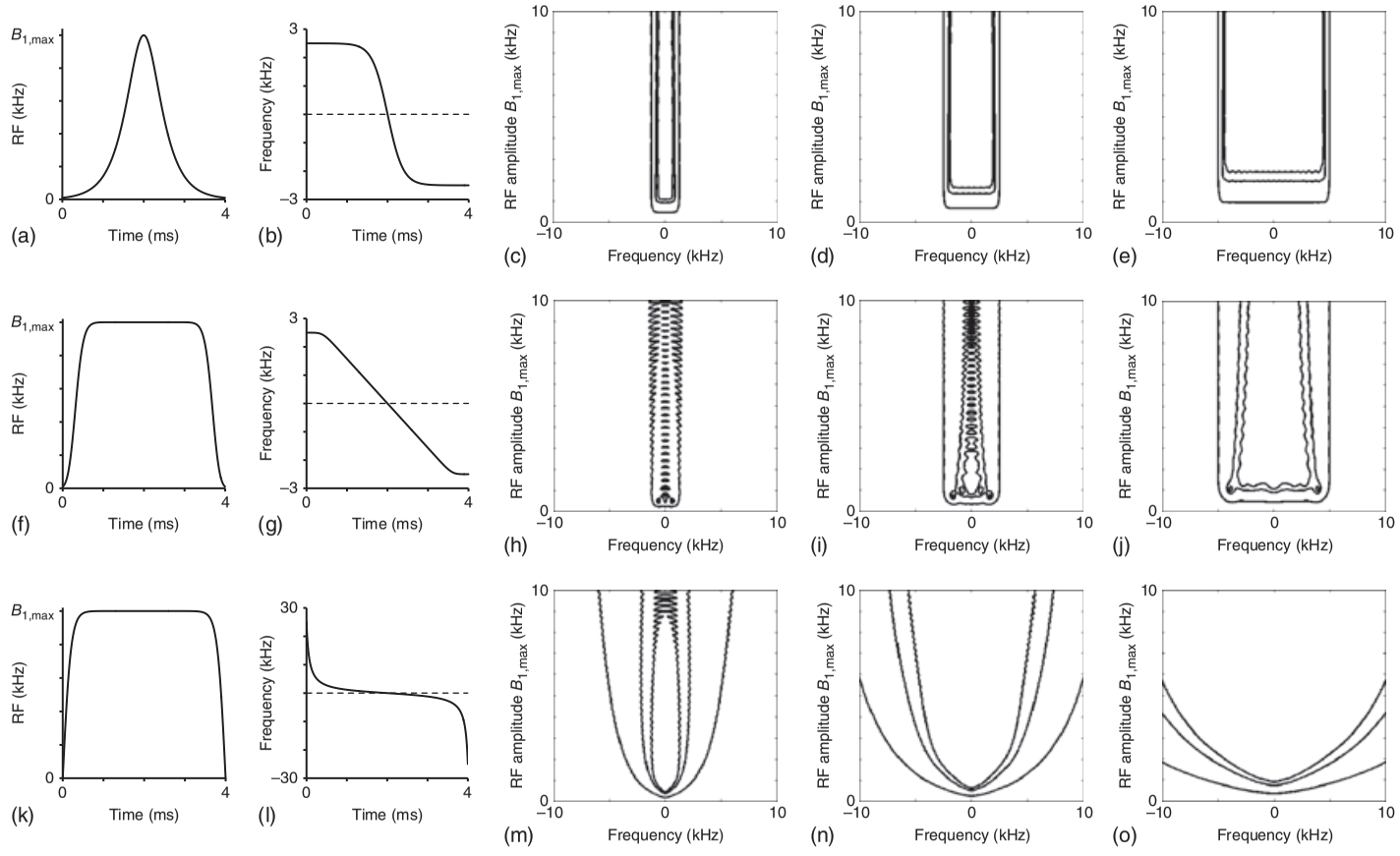

Figure 3. (a, f, k) Amplitude and (b, g, l) frequency modulation functions for (a, b) HS1 ($R = 20$), (f, g) HS8 ($R = 20$), and (k, l) NOM ($R = 200$) AFP pulses. Inversion profiles as a function of RF amplitude $B_{1,max}$ and frequency offset for (c–e) HS1, (h–j) HS8, and (m–o) NOM AFP pulses. HS1 and HS8 AFP pulses were executed with (c, h) $R = 10$, (d, i) $R = 20$, and (e, j) $R = 40$, whereas the NOM pulse was executed with (m) $R = 100$, (n) $R = 200$, and (o) $R = 400$. Contour lines are shown for $M_z/M_0 = -0.98$ (inner line), -0.90 (middle line), and 0.00 (outer line)

over wide bandwidths, whereas the HS1 and HS8 are better choices for frequency-selective inversion as required in spatial localization. The exact performance of a given AFP pulse is not easily deduced from visual inspection of the $B_1(t)$ and $\Delta\nu(t)$ modulation functions. Instead, the pulse performance should be calculated using the Bloch equations (Figure 3) or experimentally calibrated (see section titled 'Applications').

AFP Refocusing

As shown in Figures 2 and 3, AFP pulses demonstrate a superb performance for inverting longitudinal magnetization ($M_z \rightarrow -M_z$). However, other rotations such as excitation ($M_z \rightarrow M_x$) and refocusing ($M_x + iM_y \rightarrow M_x - iM_y$) are equally important for a wide range of experiments. The primary difference between M_z and M_{xy} during an AFP pulse is that M_z is initially parallel to $B_e(0)$, whereas M_{xy} is initially perpendicular to $B_e(0)$. When the effective field $B_e(t)$ rotates slowly relative to its amplitude, that is, when $|d\alpha(t)/dt| \ll |B_e(t)|$, M_z remains parallel to $B_e(t)$, which ultimately leads to spin inversion. Similarly, provided that the adiabatic condition is satisfied, M_{xy} will remain perpendicular to $B_e(t)$ throughout the pulse, leading to an inversion of the xy-plane, that is, refocusing. However, the refocusing properties are compromised as the transverse magnetization has acquired a phase angle $\beta(t)$ due to precession around $B_e(t)$ given by:

$$\beta(t) = 2\pi \int_0^t B_e(t)dt \qquad (13)$$

where $B_e(t)$ is the effective magnetic field given by equation (7). Figure 4 shows the effects of an AFP pulse on the three magnetization components M_x, M_y, and M_z. The AFP pulse achieved B_1 insensitive (Figure 4b) and frequency-selective (Figure 4c) inversion when starting with M_z before the pulse. Using M_x or M_y as a starting point before the AFP pulse will lead to B_1- and offset-dependent signal dephasing (Figure 4d and e) according to equation (13). The presence of RF inhomogeneity and different frequencies will lead to phase cancelation and signal loss.

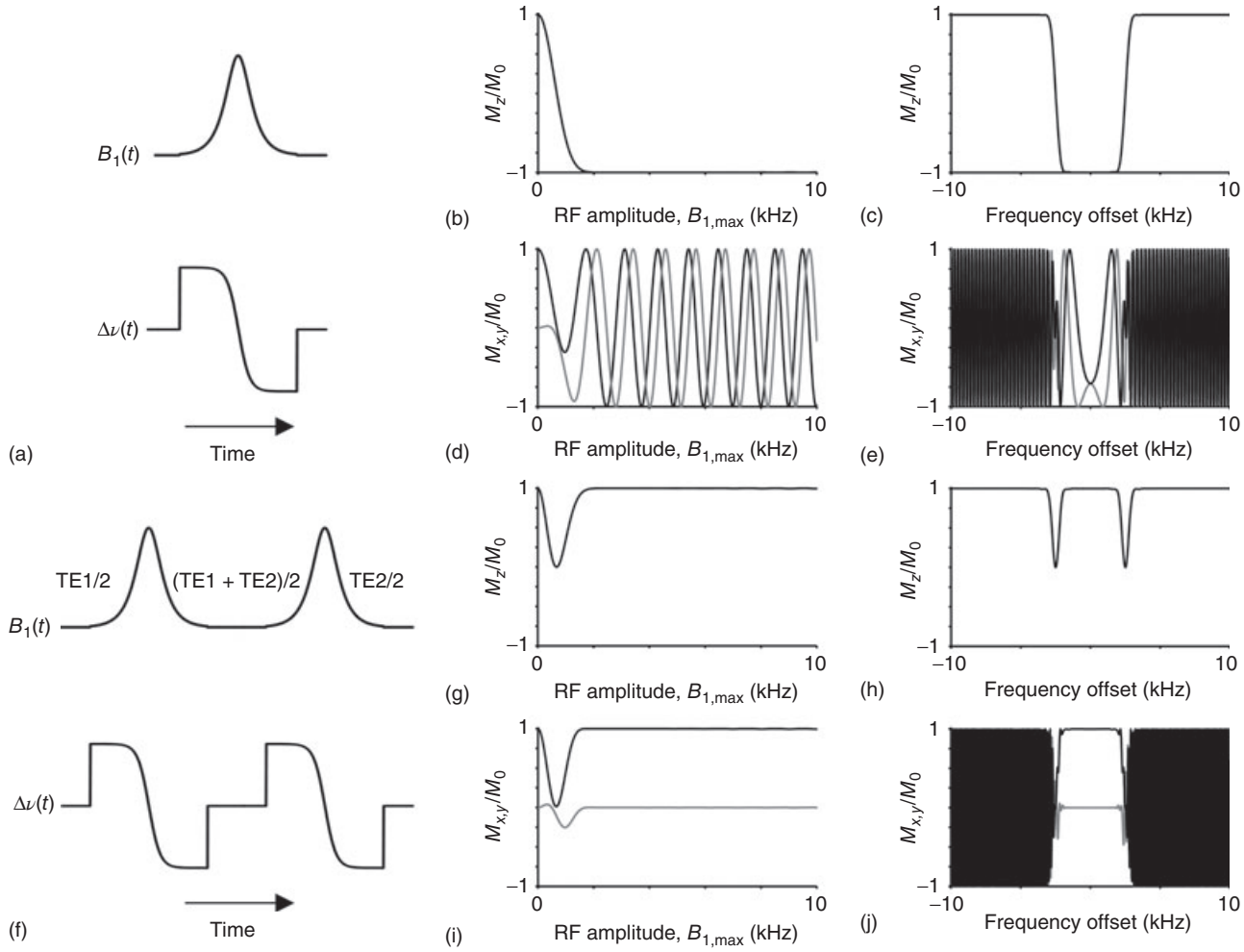

Figure 4. Inversion and refocusing properties of (a–e) single and (f–j) double AFP pulses. (a) A single AFP pulse achieves (b) B_1-independent inversion above a minimum threshold B_1 and (c) frequency-selective inversion. (d, e) Using a single AFP pulse for refocusing leads to a (d) B_1 and (e) frequency-dependent phase. (f) A double AFP pulse sequence achieves an identity (or 2π) rotation that is (g) B_1 independent and (h) frequency selective. Using the AFP pulse pair for refocusing eliminates the (i) B_1 and (j) offset-dependent phase roll

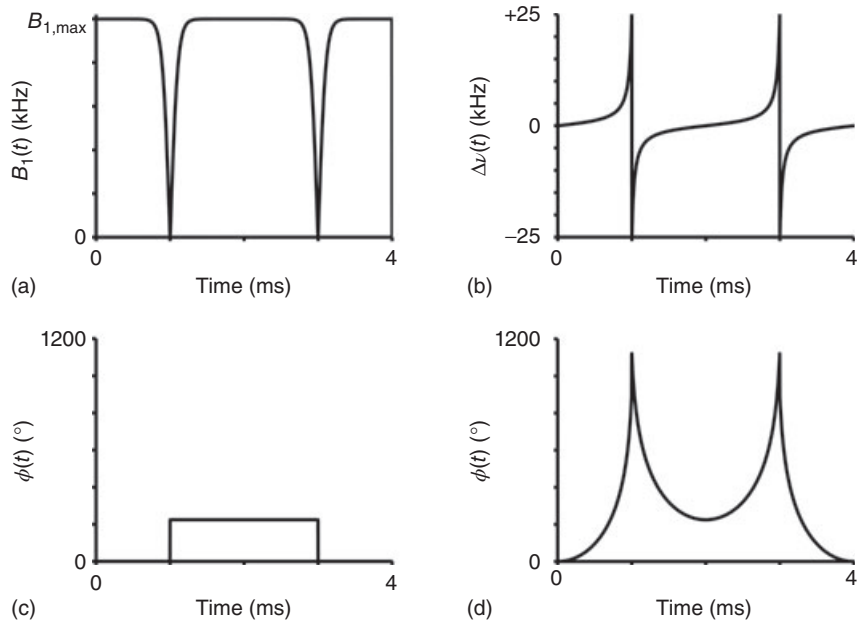

Figure 5. (a) Amplitude and (b) frequency modulations of a BIR-4 pulse, based on the modulation functions given by equations (11) and (12). (c) A phase offset of the middle two segments by $180^\circ + \theta/2$ leads to a final, B_1-independent nutation angle of θ. (d) Phase modulation obtained by numerical integration of the frequency modulation in (b) and the addition of the discrete phase jumps of (c)

In other words, a single AFP pulse is a good inversion pulse, but it is a poor choice for signal refocusing as required in a spin-echo sequence.

Conolly *et al.*[13,14] were the first to recognize that the application of additional AFP pulses could rewind the phase acquired during the first AFP pulse. After the initial description of a 3π pulse, consisting of three AFP pulses of various lengths, Conolly *et al.*[14] subsequently proposed the use of two identical AFP pulses to rewind undesirable phase accumulation. Figure 4(f) shows the pulse sequence element in which two identical AFP pulses are surrounded by delays to form a double spin-echo. The phase accumulated during the first pulse according to equation (13) is canceled by the second RF pulse, such that the transverse magnetization phase is constant as a function of RF amplitude (Figure 4i) and frequency offset (Figure 4j). For the longitudinal magnetization, the AFP pulse pair acts as a 2π pulse, bringing the magnetization back to the $+z'$-axis when the RF pulse satisfies the adiabatic condition. The AFP-based double spin-echo element provides very robust slice selection when the pulses are executed during magnetic field gradients.

Adiabatic Plane Rotation of Arbitrary Nutation Angle

As noted, AFP pulses are an excellent choice for spin inversion. While a single AFP pulse is not suitable for spin refocusing, the combination of two AFP pulses allows the formation of a perfectly refocused, frequency-selective spin-echo. When an AFP pulse is only executed until its midpoint in time, the pulse achieves B_1-insensitive excitation albeit forfeiting frequency selectivity. Unfortunately, the AFP pulse is not suitable for any other rotations that, for example, require plane rotations or arbitrary nutation angles. The B_1-insenstive rotation using 4 segments (BIR-4) pulse is a plane rotation pulse that can achieve arbitrary nutation angles with high immunity to both RF inhomogeneity and resonance offsets. BIR-4 was derived from composite pulses, which are composed of multiple hard RF pulses that compensate each other's imperfections. Garwood and Ke[12] generated a time-symmetric, composite pulse ${}^{90^\circ}_{0^\circ}{}^{180^\circ}_{180^\circ+\theta/2}{}^{90^\circ}_{0^\circ}$, which can achieve an arbitrary nutation angle θ simply by changing the phase of the center 180° pulse. The immunity toward RF inhomogeneity and frequency offset could be greatly enhanced by replacing the hard RF pulses with AFP pulse segments as shown in Figure 5. Without the phase offset for the middle two 90° segments, the pulse would simply generate an identity (or 360°) rotation. However, with a phase offset of $180^\circ + \theta/2$ for the middle two segments, an arbitrary nutation angle θ can be achieved. In addition, the time symmetry of BIR-4 ensures that the net rotation angle of the magnetization around the effective field according to equation (13) is zero, thus making BIR-4 a general purpose, plane rotation pulse. BIR-4 has found applications in MRI,[15,16] polarization transfer,[17,18] spectral editing,[19,20] T_1 relaxation measurements,[21,22] and saturation transfer.[23]

Applications

The use of adiabatic RF pulses is widespread in MRS applications. This is not surprising as many MRS studies are sensitivity limited and are therefore often performed with surface coil transceivers. The immunity of adiabatic RF pulses to RF inhomogeneity ensures maximum sensitivity, while at the same time providing convenient and user-friendly MR methods that guarantee optimal performance without subject-specific

adjustments of RF transmit power settings. Here, three MRS applications are discussed that demonstrate some of the features of adiabatic RF pulses.

3-D Spatial Localization

Image-selected in vivo spectroscopy (ISIS)[24] and localization by adiabatic spin-echo refocusing (LASER)[5,25] are two spatial localization methods that are entirely based on adiabatic RF pulses. ISIS is based on the inversion properties of AFP pulses, whereas LASER is based on the refocusing properties of AFP pulse pairs. Figure 6 shows the ISIS and LASER pulse sequences with HS1 pulses for inversion/refocusing and a BIR-4 pulse with modulations given by equations (11) and (12) for excitation. The ISIS method sequentially executes the eight on/off combinations of the three AFP pulses, which in conjunction with an appropriate receiver phase cycle leads to 3-D localization due to cancelation of signals that are not affected by all three RF pulses. Magnetic field crusher gradients following each AFP pulse ensure the elimination of spurious signals from outside the volume of interest. The main advantage of ISIS localization is that it can be placed before any excitation sequence, enabling very short or zero echo-time acquisitions. The primary disadvantage is that multiple scans are required to achieve 3-D localization, thereby introducing sensitivity to subject motion and to system instability.

In 3-D LASER (Figure 6b), the AFP pulses are executed following excitation, permitting single-scan 3-D localization at the cost of a longer, minimum echo time (TE). On animal scanners, the minimum TE is often determined by the available RF peak power and gradient slew rates, which typically accumulate to TE_{min} values of 15 ms or less. On high-field human scanners, the minimum TE is often dictated by RF power deposition making TE_{min} 50 ms or longer. In order to reduce TE while still retaining most of the 3-D LASER benefits,

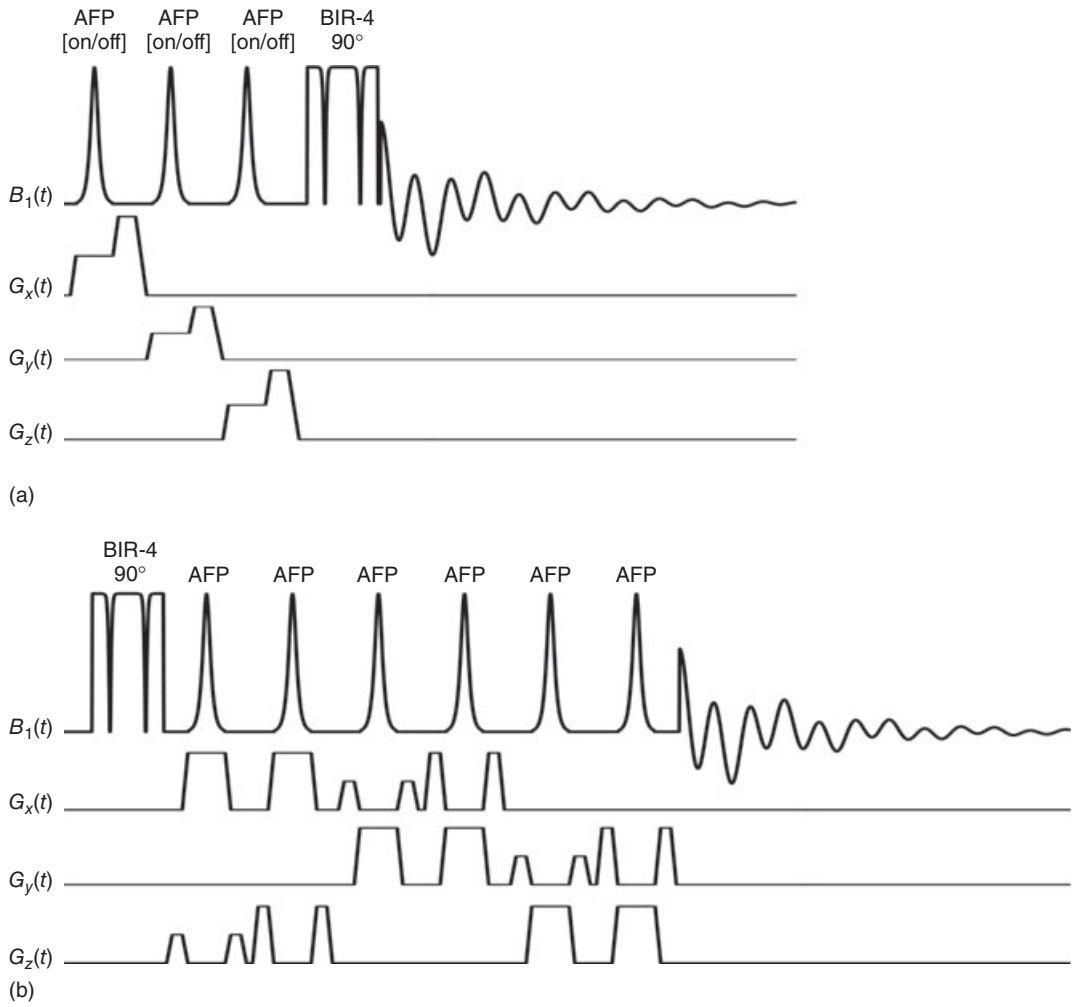

Figure 6. 3-D spatial localization methods based on AFP pulses. (a) ISIS and (b) LASER. (a) The ISIS sequence requires a minimum of eight acquisitions to execute all on/off combinations of the three AFP pulses in order to achieve complete 3-D localization. During the off condition, the gradients are retained to keep the eddy current response identical for all acquisitions. As localization is achieved based on the longitudinal magnetization, any excitation pulse sequence can follow the ISIS module. (b) LASER is based on the refocusing properties of AFP pulse pairs (Figure 4). By executing three AFP pulse pairs along orthogonal directions, complete 3-D localization is achieved in a single acquisition. Surrounding each AFP pulse with unique crusher gradients is essential for eliminating artifacts

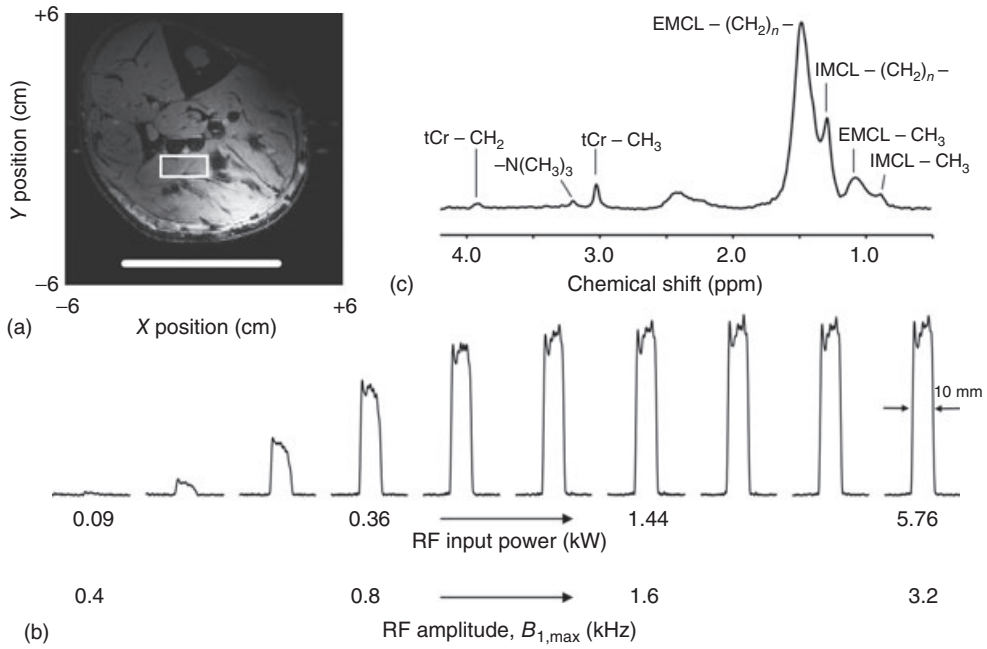

Figure 7. (a) MR image of the human leg at 7 T indicating a 25 mm × 10 mm × 20 mm volume and an 80 mm diameter surface coil transceiver. (b) Calibration of the AFP pulse power (6 ms HS1, $R = 20$) on 1-D spatial profiles. The RF power increases in steps of 2 dB, leading to a doubling of $B_{1,\max}$ every three profiles. The signal from the 3-D localized volume increases with increasing RF power until the adiabatic condition is adequately satisfied ($B_{1,\max} \sim 1.2$ kHz). Increasing the RF power further does not lead to improved performance but does increase the RF power deposition. (c) 3-D LASER ^{1}H MR spectrum obtained without any secondary localization technique (TR = 4000 ms, TE = 150 ms, NA = 64)

the semi-LASER sequence has been described[26,27] in which one pair of AFP pulses is eliminated and replaced by a slice-selective (but non-adiabatic) excitation pulse.

Figure 7 shows a practical example of ^{1}H MRS based on 3-D LASER localization on the human leg at 7 T. A visually intuitive and straightforward manner to calibrate the AFP pulses is to extend the LASER sequence with a readout gradient during signal acquisition. Fourier transformation of the gradient-echo signal provides a 1-D spatial profile of the localized volume along the selected direction. Increasing the RF power (Figure 7b) brings the AFP pulses closer to the point where the adiabatic condition, equation (7), is adequately satisfied. At about 0.9 kW, the intensity of the spatial profile levels off, indicating that the adiabatic RF pulses have reached the minimum threshold to satisfy the adiabatic condition. Increasing the transmit power increases the power deposition without any further benefit in sensitivity or localization quality. It is therefore advisable to set the transmit power 1–2 dB above the minimum threshold power to ensure that the spatial localization quality is maintained on all subjects, despite small differences in RF coil performance. It should be noted that the power requirements for the 3-D LASER AFP refocusing and BIR-4 excitation pulses are most likely different, just as the performance of AFP pulses varies with different modulation functions (Figure 3). It is therefore advisable to calibrate the AFP pulse power first (at a constant excitation pulse power), after which the BIR-4 pulse power can be calibrated. Further note that while a BIR-4 pulse may work satisfactorily on-resonance at low RF power, it may require substantially more RF power to achieve the desired nutation angle over the full spectral width.

Outer Volume Suppression

Spatial localization is an important component of any MRS study and adiabatic RF pulses can be utilized in a number of them as described for ISIS and LASER. For relatively homogenous 'volume' coils, non-adiabatic localization methods such as stimulated echo acquisition mode (STEAM)[28] and point-resolved spectroscopy (PRESS)[29] can provide reasonable localization at short TE values without high RF power deposition. However, modest RF inhomogeneity, imperfect RF pulse profiles, and finite T_1 relaxation times can all compromise localization performance. In these cases, localization can be significantly improved by employing a secondary localization method such as outer volume suppression (OVS).

OVS is achieved with a frequency-selective excitation pulse followed by a magnetic field crusher gradient. Figure 8(a) shows the OVS performance of a 1 ms conventional, amplitude-modulated SLR pulse at $B_{1,\max} = 1.5$ kHz. As the nutation angle of a single pulse is close to 90°, the OVS performance is good and covers about 6.0 kHz. As the OVS module is repeated three times to enhance the insensitivity to RF inhomogeneity, a slight mismatch (of up to ±10%) of the 90° nutation angle does not severely compromise the OVS performance. Figure 8(a) also shows the OVS performance of a 1-ms HS4 pulse ($R = 20$) at $B_{1,\max} = 1.5$ kHz. While OVS based on HS4 pulses executed under nonadiabatic conditions has the same sensitivity toward RF inhomogeneity as the SLR-based OVS shown in Figure 8(a),

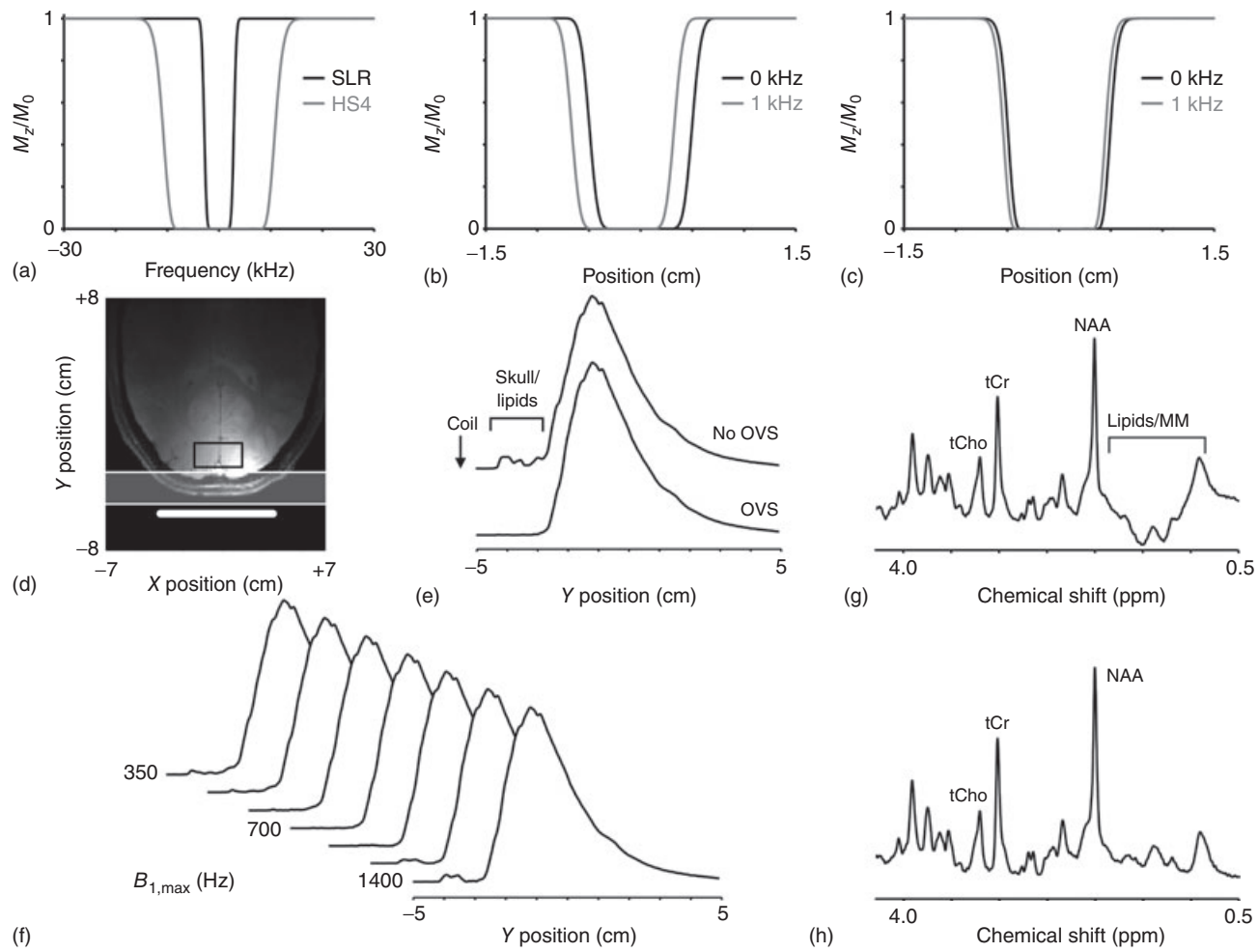

Figure 8. Outer volume suppression based on AFP pulses. (a) At an identical maximum RF amplitude $B_{1,max}$ of 1.5 kHz, an AFP pulse (HS4, 1 ms, $R = 20$) can achieve excitation of a >20 kHz bandwidth, almost four times as large of that obtained with a conventional SLR excitation pulse. (b, c) The chemical shift displacement of lipids (black line) relative to water (gray line) will reduce from about 20% of the slice width for the (b) SLR pulse to about 5% for the (c) HS4 pulse. (d) MR image obtained with an 80 mm diameter surface coil indicating the 3-D STEAM volume (30 mm × 15 mm × 20 mm) and the OVS slice (20 mm thick). (e) 1-D spatial profile along the Y dimension perpendicular to the surface coil transceiver. The STEAM slice selection in the Y direction was removed in order to visualize the water and lipid signals in the skull region (top trace). With optimal transmit power settings, the AFP-based OVS removes all signals from the skull without affecting the brain signal (bottom trace). (f) Power calibration of the OVS based on 2 ms HS4 ($R = 20$) AFP pulses. As the AFP pulses are operating in a non-adiabatic power regime, the OVS performance improves up to $B_{1,max} \sim 700$ Hz after which it deteriorates with higher power settings. The profiles are acquired at power settings separated by 2 dB units. (g, h) 3-D STEAM ^{1}H MR spectra obtained (g) without and (h) with AFP-based OVS (TR = 4000 ms, TE = 20 ms, NA = 64)

there are two distinct advantages for using HSn pulses for OVS. First, as discussed previously[6,30] the frequency-selective profile of HSn pulses remains constant even when executed in a non-adiabatic power regime. As such, the OVS slice profile is well behaved despite the presence of strong RF inhomogeneity. For most amplitude-modulated pulses, the frequency-selective profile greatly deteriorates when the nutation angle deviates from the range for which the pulse was optimized. In those cases, the OVS slice profile can be heavily distorted and even suppress desirable signals. Second, at the same maximum RF amplitude of 1.5 kHz, the HS4 pulse achieves >20 kHz bandwidth, more than three times that achieved by the SLR-based OVS. This increased bandwidth reduces chemical shift displacement artifacts, which are especially prominent at high magnetic fields (Figure 8b and c).

Figure 8(e) shows 1-D spatial profiles of the human brain at 7 T (Figure 8(d)) along the Y direction, perpendicular to the plane of the surface coil transceiver. The spatial profile shows clear signals from water and lipids in the skull region that are largely removed with OVS without affecting the brain signal. Experimental calibration of OVS transmit power (Figure 8f) is similar to that of the LASER AFP pulses with the exception that the OVS pulses behave non-adiabatically. Therefore, the OVS performance does not level off, but rather hits a maximum before deteriorating at higher power levels. The immunity of the non-adiabatic OVS module can be increased by repeating the OVS modules or by imposing additional amplitude modulation between the OVS modules.[30] Figure 8(g) shows a 3-D STEAM-localized ^{1}H NMR spectrum from the human brain at 7 T without OVS as a secondary localization method. The spectral

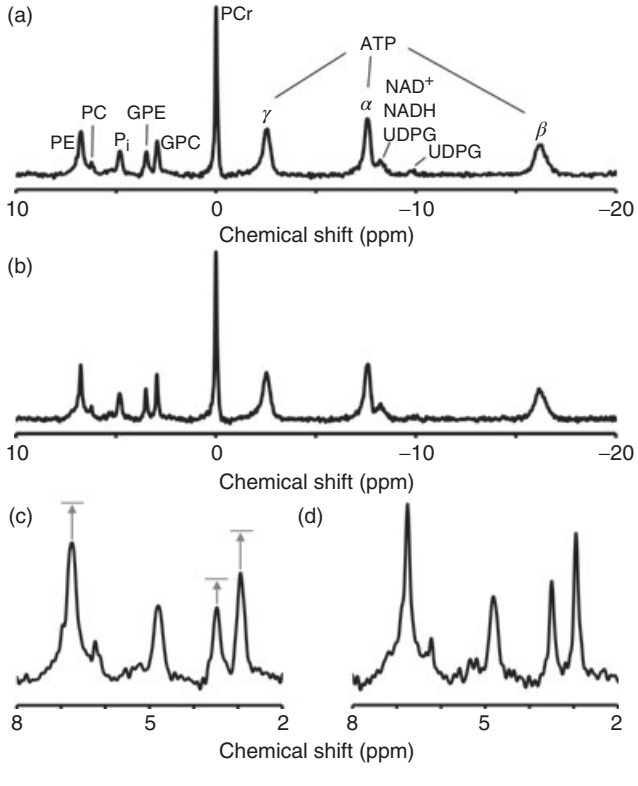

Figure 9. Adiabatic ^{1}H decoupling during ^{31}P MRS of the human brain at 7 T. ^{31}P MR spectra obtained (a, c) without and (b, d) with adiabatic ^{1}H decoupling. The decoupling scheme is based on 8 ms HS4 pulses executed at $B_{1,\max} \sim 0.3$ kHz ($R = 10$). The signals from phospho-monoesters, PC and PE, and phospho-di-esters, GPC and GPE, demonstrate a noticeable improvement in spectral resolution. Signals from P_i, PCr, ATP, and NAD^+/NADH do not show a significant effect either due to the absence of ^{1}H-^{31}P scalar coupling (P_i and PCr) or due to the short T_2 relaxation time constants and hence broad lines (ATP and NAD^+/NADH)

quality is high as judged by the narrow spectral lines and the high sensitivity. However, visible artifacts from extracranial lipids are visible in the 1.0–2.0 ppm region. These lipid signals obscure signals from lactate and alanine and may even compromise the rest of the spectrum when sufficiently intense. Figure 8(h) shows the same spectrum acquired in the presence of complementary HSn-based OVS modules. The majority of the spectrum is unaffected, but the artifactual lipid signals have been suppressed to below the spectral noise floor.

Heteronuclear Decoupling

Broadband decoupling in heteronuclear NMR is a valuable technique to enhance sensitivity and achieve spectral simplification. Heteronuclear decoupling based on composite pulses built into a decoupling super cycle is still the most popular choice for in vivo applications. However, composite pulse decoupling has a limited bandwidth, is dependent on the RF power, and may randomly affect signal outside the decoupling bandwidth. Broadband decoupling based on adiabatic RF pulses was proposed for in vivo phosphorus-31 (^{31}P) NMR by Luyten *et al.*[31] It gained enormous popularity in high-resolution, liquid-state NMR when composite decoupling was no longer able to accommodate the large bandwidths encountered at very high magnetic fields.[32–34] On high-field animal MR scanners, adiabatic RF pulses are a necessity to achieve broadband carbon (^{13}C) decoupling during proton (^{1}H) MRS.[35] Unfortunately, high RF power deposition prevents the use of adiabatic RF pulses on high-field human scanners for broadband ^{13}C decoupling.[36] The smaller scalar couplings associated with ^{31}P NMR allow for longer adiabatic RF pulses, thereby greatly reducing the RF power requirements.

Figure 9 shows adiabatic ^{1}H decoupling based on 8 ms HS4 ($R = 10$) pulses applied to ^{31}P NMR of the human brain at 7 T. The decoupling pulses are incorporated into a 20-step supercycle designed to minimize decoupling sidebands.[36] It can be seen that the phosphomonoester signals of phosphocholine (PC) and phosphoethanolamine (PE) and phosphodiester signals of glycerol-phosphocholine (GPC) and glycerol-phosphoethanolamine (GPE) sharpen up significantly due to the removal of the ^{1}H–^{31}P scalar coupling splittings. While the α-ATP, NAD^+, and NADH resonances also have extensive ^{1}H–^{31}P scalar couplings, the multiplets do not exhibit significant sharpening, likely due to the short T_2^* relaxation time constants. In this example, adiabatic RF pulses were primarily used for their improved off-resonance performance at low peak power. The immunity toward RF inhomogeneity provided a level of convenience, but was less critical for the final result.

Biographical Sketch

Robin A. de Graaf. b. 1970. BA, 1994, PhD, 1998, University of Utrecht, The Netherlands. As a graduate student, he worked on adiabatic RF pulse design. Published a monograph on In Vivo NMR Spectroscopy in 1998 (second revision 2007). Moved to Yale University, USA, in 1999 to work on metabolic flux mapping using ^{13}C MR spectroscopy. He is currently an Associate Professor in the Department of Radiology and Biomedical Imaging with research interests in MR spectroscopy, MR hardware, and high-field MR applications.

Related Articles

Complex Radiofrequency Pulses; Composite Pulses; Decoupling Methods; Proton Decoupling During In Vivo Whole Body Phosphorus MRS; Proton Decoupling in Whole Body Carbon-13 MRS; Selective Pulses; Shaped Pulses; Single Voxel Localized Proton NMR Spectroscopy of Human Brain In Vivo; Garwood, Michael: Frequency-Modulated Pulses in the Early Days of Biomedical NMR; Kupče, Ēriks: Reflections, Projections and Adiabatic Passages; Ordidge, Roger: MRS Spatial Localization Using Selective RF Pulses

References

1. J. Pauly, P. Le Roux, D. Nishimura, and A. Macovski, *IEEE Trans. Med. Imaging*, 1991, **10**, 53.
2. F. Bloch, *Phys. Rev.*, 1946, **70**, 460.
3. E. M. Purcell, H. C. Torrey, and R. V. Pound, *Phys. Rev.*, 1946, **69**, 37.
4. R. A. de Graaf and K. Nicolay, *Concepts Magn. Reson.*, 1997, **9**, 247.
5. M. Garwood and L. DelaBarre, *J. Magn. Reson.*, 2001, **153**, 155.
6. R. A. de Graaf, *In Vivo* NMR Spectroscopy. Principles and Techniques, 2nd edn, John Wiley & Sons, Ltd: Chichester, 2007.

7. M. S. Silver, R. I. Joseph, and D. I. Hoult, *J. Magn. Reson.*, 1984, **59**, 347.
8. F. T. Hioe, *Phys. Rev. A*, 1984, **30**, 2100.
9. K. Ugurbil, M. Garwood, and A. R. Rath, *J. Magn. Reson.*, 1988, **80**, 448.
10. A. Tannus and M. Garwood, *J. Magn. Reson. Ser. A*, 1996, **120**, 133.
11. A. Tannus and M. Garwood, *NMR Biomed.*, 1997, **10**, 423.
12. M. Garwood and Y. Ke, *J. Magn. Reson.*, 1991, **94**, 511.
13. S. Conolly, D. Nishimura, and A. Macovski, *J. Magn. Reson.*, 1989, **83**, 324.
14. S. Conolly, G. Glover, D. Nishimura, and A. Macovski, *Magn. Reson. Med.*, 1991, **18**, 28.
15. R. S. Staewen, A. J. Johnson, B. D. Ross, T. Parrish, H. Merkle, and M. Garwood, *Invest. Radiol.*, 1990, **25**, 559.
16. R. A. de Graaf, D. L. Rothman, and K. L. Behar, *NMR Biomed.*, 2003, **16**, 29.
17. H. Merkle, H. Wei, M. Garwood, and K. Ugurbil, *J. Magn. Reson.*, 1992, **99**, 480.
18. J. Shen, K. F. Petersen, K. L. Behar, P. Brown, T. W. Nixon, G. F. Mason, O. A. Petroff, G. I. Shulman, R. G. Shulman, and D. L. Rothman, *Proc. Natl. Acad. Sci. U. S. A.*, 1999, **96**, 8235.
19. M. Garwood and H. Merkle, *J. Magn. Reson.*, 1991, **94**, 180.
20. R. A. de Graaf, Y. Luo, M. Terpstra, and M. Garwood, *J. Magn. Reson. Ser. B*, 1995, **109**, 184.
21. H. Sakuma, S. J. Nelson, D. B. Vigneron, J. Hartiala, and C. B. Higgins, *Magn. Reson. Med.*, 2005, **29**, 688.
22. P. A. Bottomley and R. Ouwerkerk, *J. Magn. Reson. Ser. B*, 1994, **104**, 159.
23. P. A. Bottomley, R. Ouwerkerk, R. F. Lee, and R. G. Weiss, *Magn. Reson. Med.*, 2002, **47**, 850.
24. R. J. Ordidge, A. Connelly, and J. A. Lohman, *J. Magn. Reson.*, 1986, **66**, 283.
25. J. Slotboom, A. F. Mehlkopf, and W. M. Bovee, *J. Magn. Reson.*, 1991, **95**, 396.
26. T. W. Scheenen, A. Heerschap, and D. W. Klomp, *MAGMA*, 2008, **21**, 95.
27. T. W. Scheenen, D. W. Klomp, J. P. Wijnen, and A. Heerschap, *Magn. Reson. Med.*, 2008, **59**, 1.
28. J. Frahm, K. D. Merboldt, and W. Hanicke, *J. Magn. Reson.*, 1987, **72**, 502.
29. P. A. Bottomley, *Ann. N. Y. Acad. Sci.*, 1987, **508**, 333.
30. Y. Luo, R. A. de Graaf, L. DelaBarre, A. Tannus, and M. Garwood, *Magn. Reson. Med.*, 2001, **45**, 1095.
31. P. R. Luyten, G. Bruntink, F. M. Sloff, J. W. Vermeulen, J. I. van der Heijden, J. A. den Hollander, and A. Heerschap, *NMR Biomed.*, 1989, **1**, 177.
32. M. R. Bendall, *J. Magn. Reson. Ser. A*, 1995, **112**, 126.
33. E. Kupce and R. Freeman, *J. Magn. Reson. Ser. A*, 1995, **115**, 273.
34. Z. Starcuk, K. Bartusek, and Z. Starcuk, *J. Magn. Reson. Ser. A*, 1994, **107**, 24.
35. P. van Eijsden, K. L. Behar, G. F. Mason, K. P. J. Braun, and R. A. de Graaf, *J. Neurochem.*, 2010, **112**, 24.
36. R. A. de Graaf, *Magn. Reson. Med.*, 2005, **53**, 1297.